THE JOURNAL OF PHYSICAL CHEMISTRY Letters

Letter

Cite This: J. Phys. Chem. Lett. 2019, 10, 7179−7187

pubs.acs.org/JPCL

Electron−Phonon Scattering Is Much Weaker in Carbon Nanotubes than in Graphene Nanoribbons

Guoqing Zhou,[†,‡] Chao Cen,[†] Shuyi Wang,[†] Mingsen Deng,[*,†] and Oleg V. Prezhdo[*,‡,§]

[†]Guizhou Provincial Key Laboratory of Computational Nano-material Science, Guizhou Education University, Guiyang 550018, China

[‡]Department of Physics and Astronomy, University of Southern California, Los Angeles, California 90089, United States

[§]Department of Chemistry, University of Southern California, Los Angeles, California 90089, United States

ABSTRACT: Carbon nanotubes (CNTs) and graphene nanoribbons (GNRs) are lower-dimensional derivatives of graphene. Similar to graphene, they exhibit high charge mobilities; however, in contrast to graphene, they are semiconducting and thus are suitable for electronics, optics, solar energy devices, and other applications. Charge carrier mobilities, energies, and lifetimes are governed by scattering with phonons, and we demonstrate, using ab initio nonadiabatic molecular dynamics, that charge−phonon scattering is much stronger in GNRs. Focusing on a GNR and a CNT of similar size and electronic properties, we show that the difference arises because of the significantly higher stiffness of the CNT. The GNR undergoes large-scale undulating motions at ambient conditions. Such thermal geometry distortions localize wave functions, accelerate both elastic and inelastic charge−phonon scattering, and increase the rates of energy and carrier losses. Even though, formally, both CNTs and GNRs are quantum confined derivatives of graphene, charge−phonon scattering differs significantly between them. Showing good agreement with time-resolved photoconductivity and photoluminescence measurements, the study demonstrates that GNRs are quite similar to molecules, such as conjugated polymers, while CNTs exhibit extended features attributed to bulk materials. The state-of-the-art simulations alter the traditional view of graphene nanostructures and demonstrate that the performance can be tuned not only by size and composition but also by stiffness and response to thermal excitation.

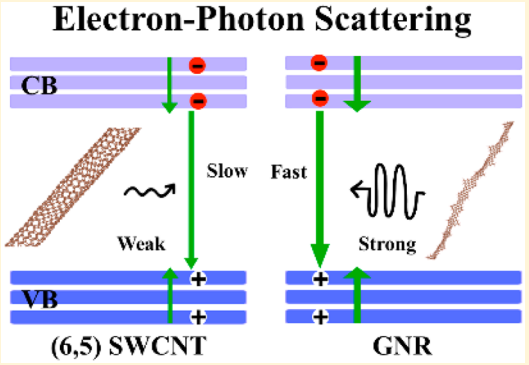

Downloaded via UNIV OF SOUTHERN CALIFORNIA on April 4, 2020 at 07:12:14 (UTC).
See https://pubs.acs.org/sharingguidelines for options on how to legitimately share published articles.

Graphene has been attracting attention for over a decade because of its unique structure and extraordinary electronic, photonic, electric, mechanical and chemical properties.[1−4] With the thickness reduced to the single-atom limit, and the inversion and time-reversal symmetries, the two-dimensional system exhibits a Dirac cone in its electronic structure, which leads to a vanishing bandgap and massless charge carriers with very high mobilities.[1] However, the gapless band structure hinders graphene applications in optics, electronics, and photovoltaics, which require semiconducting properties.

In order to create a semiconductor bandgap, one can apply the idea of quantum confinements, giving rise to two types of one-dimensional graphene-based nanostructures: carbon nanotubes (CNTs) and graphene nanoribbons (GNRs). CNTs were characterized[5] a decade before the isolation of single-layer graphene.[1] Conceptually, a CNT can be viewed as a graphene derivative in which the atom-thick sheet is rolled up and connected along a particular lattice vector.[6,7] Depending on the lattice vector, CNTs can be metallic or semiconducting, with varying diameters, energy gaps, stiffness, and other properties, forming a rich family of structures. Synthetically, CNTs are created by various methods, including arc discharge, lasers, and catalyzed chemical vapor deposition.[6,8,9] These tubular structures can form bundles or can be isolated into multiwalled and single-walled CNTs (SWCNTs). Current synthesis and purification technologies have a high degree of selectivity for CNT size, type, and chirality.[10] Planar GNRs can be viewed as nanometer-wide strips of graphene or as conjugated polymers made of wide repeat units. GNRs can be fabricated top-down by lithographic etching of graphene and CNT unzipping, as well as bottom-up through on-surface or solution-based synthesis.[11,12] By tailoring the chirality and diameters of CNTs, as well as widths and edges of GNRs, one can control bandgaps and design many fruitful structures,[13,14] leading to a wide range of applications in electronics,[15,16] electrochemical energy storage,[13,17,18] hydrogen storage,[19−21] photovoltaics,[22,23] electrochemical sensing,[24] etc.

Applications of CNTs and GNRs depend strongly on their ability to transport charges. In turn, charge transport is governed by charge-scattering processes, among which electron−phonon scattering constitutes the main mechanism

Received: September 28, 2019
Accepted: October 23, 2019
Published: October 23, 2019

© 2019 American Chemical Society

DOI: 10.1021/acs.jpclett.9b02874
J. Phys. Chem. Lett. 2019, 10, 7179−7187

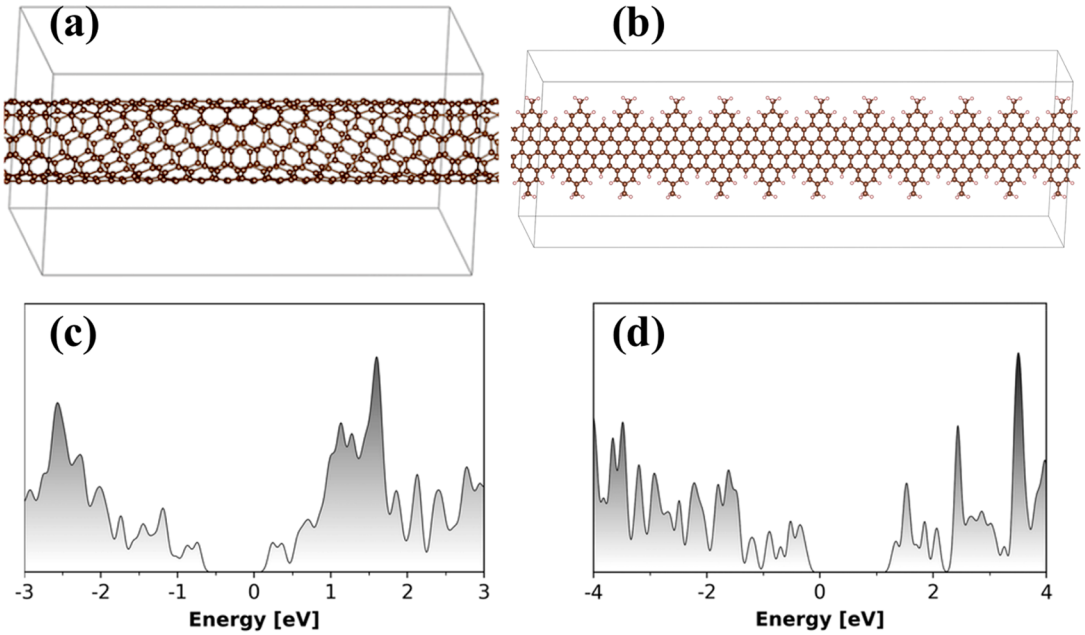

Figure 1. Simulation cells showing optimized structures of (a) (6,5) single-wall carbon nanotube (SWCNT) and (b) graphene nanoribbon (GNR). The SWCNT has 364 carbon atoms, and the GNR has 352 carbon and 132 hydrogen atoms. Electronic density of states for (c) SWCNT and (d) GNR.

of charge and energy losses to heat. Multiple time-resolved spectroscopic experiments and a few simulations have been carried out in order to characterize charge scattering in CNTs and GNRs, including both carrier−carrier and carrier−phonon scattering.[25−41] It has been demonstrated that energetic charge carriers in CNTs couple to the high-frequency G-modes, while charges with lower energies couple to lower-frequency radial breathing (RBM) vibrations. Atomic and boundary defects, as well as CNT ends, are known to contribute significantly to nonradiative charge−phonon relaxation, because CNTs are very good conductors and charges can easily reach defect sites. Charge transport in GNRs is strongly influenced by edges, because edges are susceptible to distortion and facilitate formation of localized charge carriers, known as polarons, which exhibit different transport properties than free carriers.[42,43]

Particularly interesting is the work of Bonn and co-workers,[25] because it provides a direct comparison between a CNT and a GNR of similar size, using the same experimental tools. Such comparison gives an opportunity to understand and characterize the similarities and differences between these seeminly analogous nanostructures, which can be converted between each other. In particular, Bonn and co-workers measure time-resolved photoconductivity of CNTs and GNRs and show that electron−phonon scattering events are more frequent in GNRs, and as a result, the conductivity decays several times faster in GNRs than CNTs. These[25] as well as many other[26−31] time-resolved experiments are most closely mimicked by nonadiabatic (NA) molecular dynamics (MD) techniques, developed initially[44] in the 1960s and 1970s to study gas-phase and surface scattering processes and adapted later[45−48] to condensed-phase systems. Our group developed several NAMD approaches[48−53] designed specifically for nanoscale systems and implemented them within time-dependent density functional theory (TDDFT).[54−56]

In this Letter, we employ large-scale ab initio NAMD to demonstrate that charge−phonon scattering is much faster in a GNR than in a CNT of similar size and bandgap. Even though both systems are formally quantum confined derivaties of graphene and exhibit similar electronic structure at 0 K, their properties differ significantly at room temperature. GNRs are much more flexible than CNTs and undergo significant geometry distortions at ambient conditions. The distortions localize electron and hole wave functions and enhance both inelastic and elastic charge−phonon scattering, which determine charge momentum, energy, and lifetime. The large unharmonicities exhibited by GNRs, as well as the presence of light H atoms at the edges, broaden the spectrum of vibrational motions that couple to charges. The NA electron−phonon coupling is an order of magnitude stronger in the GNR, and the nonradiative electron−hole recombination is significantly faster. Nearly identical at first glance, CNTs exhibit features associated with bulk materials, while GNRs show properties that are much more molecular. The reported results show good agreement with the time-resolved photoconductivity and photoluminescence measurements, provide a detailed atomistic picture and unique insights into the charge−phonon dynamics in graphene nanostructures, and suggest that controlling the rigidity of one-dimensional nanostructures can be used to tune their performance.

The study focuses on the two graphene nanostructures investigated experimentally by Jensen et al.,[25] namely, the (6,5) SWCNT and GNR, as shown in Figure 1a,b. For computational efficiency, the $-C_{12}H_{25}$ alkyl side chains in the GNR are replaced with the short methyl groups, $-CH_3$. The (6,5) SWCNT is represented by a $1 \times 1 \times 1$ unit cell containing 364 C atoms. The simulation cell of the GNR contains 11 unit cells, $1 \times 1 \times 11$, with a total of 352 C atoms and 132 H atoms. The system sizes are chosen to be similar to facilitate direct comparison of the simulation results, such as densities of states (DOS) and phonon modes involved in the nonradiative relaxation. To eliminate spurious interactions between periodic images and to represent isolated systems, 10 Å of vacuum are

DOI: 10.1021/acs.jpclett.9b02874
J. Phys. Chem. Lett. 2019, 10, 7179−7187

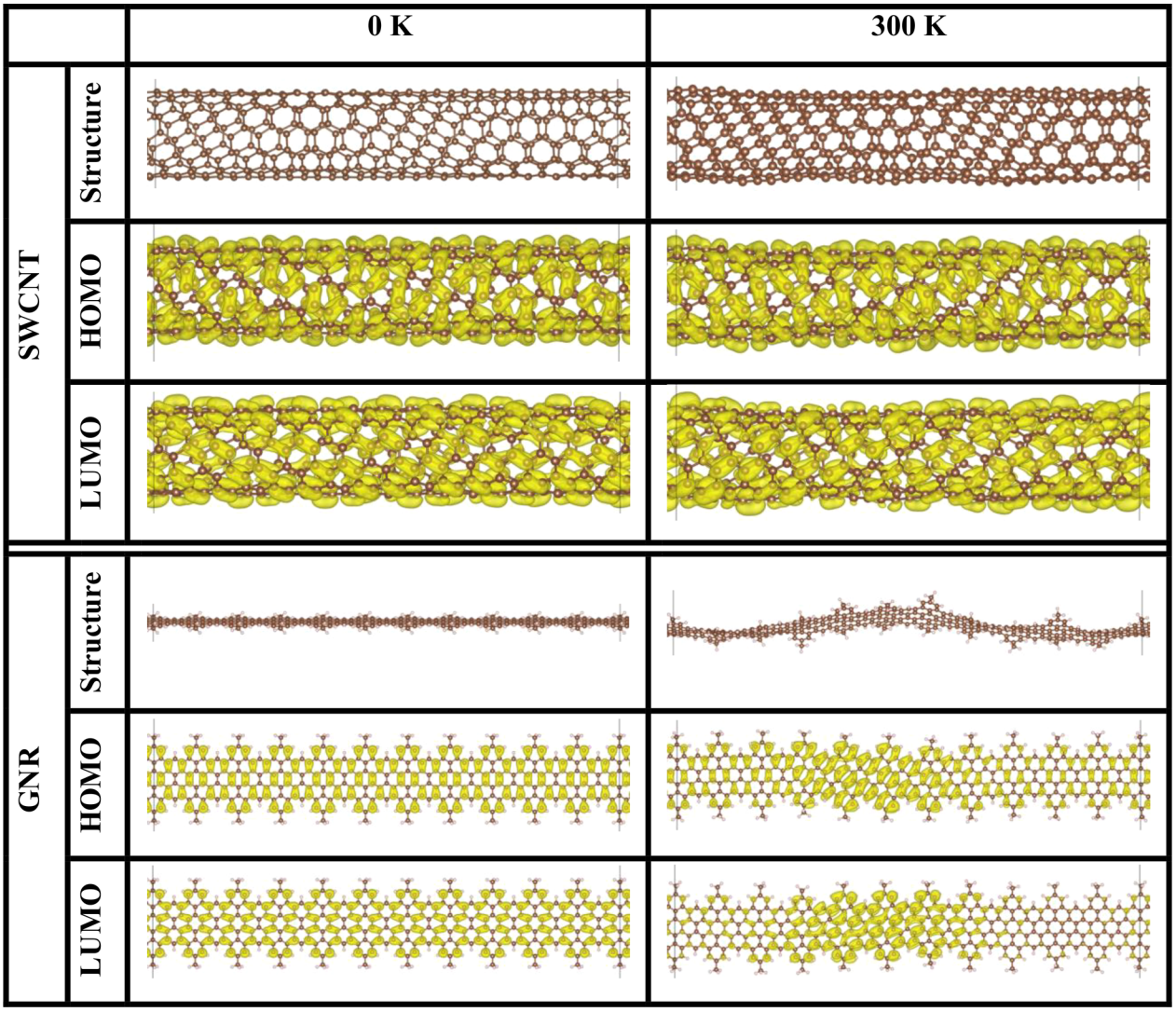

Figure 2. Geometric structure and HOMO and LUMO density distributions of the SWCNT and GNR at 0 and 300 K. The perfect periodic structures of the SWCNT and GNR are distorted at the finite temperature. The distortion is much more significant for the GNR, because it is less rigid. Importantly, the HOMO and LUMO densities become notably localized in the GNR at ambient temperature, while they remain delocalized in the SWCNT.

added in the two directions perpendicular to the longitudinal axis of the SWCNT and GNR.

The geometric structure optimization and adiabatic MD simulations are performed with the Vienna Ab initio Simulation Package (VASP),[57] employing the Perdew–Burke–Ernzerhof (PBE) exchange–correlation functional[58] and the projector augmented wave (PAW) method.[59] The Γ-point is used to sample the Brillouin zone of both systems, because their atomistic representation is already large, involving over 350 C atoms in each case. The optimized structures of the SWCNT and GNR have the bandgaps of 0.97 and 1.51 eV, respectively, relatively close to the experimental values of 1.17 and 1.88 eV.[25] The bandgaps are underestimated because of the well-known self-interaction error of pure DFT functionals, such as PBE. Subsequently during the NAMD simulations we scale the PBE bandgaps to the experimental values.

After the geometry optimization, the systems are heated to 300 K with the Nosé–Hoover thermostat and thermalized for 2 ps. Then, 5 ps microcanonical trajectories are generated with a 1 fs time step. The trajectories are used to perform NAMD using the in-house version of the PYthon eXtension for Ab Initio Dynamics (PYXAID) code,[55,56] interfaced with VASP.[57] The intraband charge–phonon relaxation is studied using fewest switches surface hopping (FSSH),[45] which is the most popular NAMD approach. The nonradiative electron–hole recombination is investigated using decoherence-induced surface hopping (DISH),[50] which incorporates quantum decoherence effects and produces hops at decoherence events using the standard quantum mechanical probabilities, rather than ad hoc transition probabilities such as in FSSH. FSSH is suitable to model quantum dynamics in which transitions either occur locally in time or space, e.g. near avoided crossings, or are faster than loss of quantum coherence, such as during intraband relaxation involving dense manifolds of states. Inclusion of decoherence effects via DISH, or other methods such as decoherence corrected FSSH,[33,46] is required to model transitions that are much slower than decoherence time,[60] e.g. transitions across large energy gaps leading to electron–hole recombination. The classical path approximation (CPA) is implemented for both FSSH[55] and DISH,[56] under the assumption that thermal fluctuations in the atomic coordinates

DOI: 10.1021/acs.jpclett.9b02874
J. Phys. Chem. Lett. 2019, 10, 7179–7187

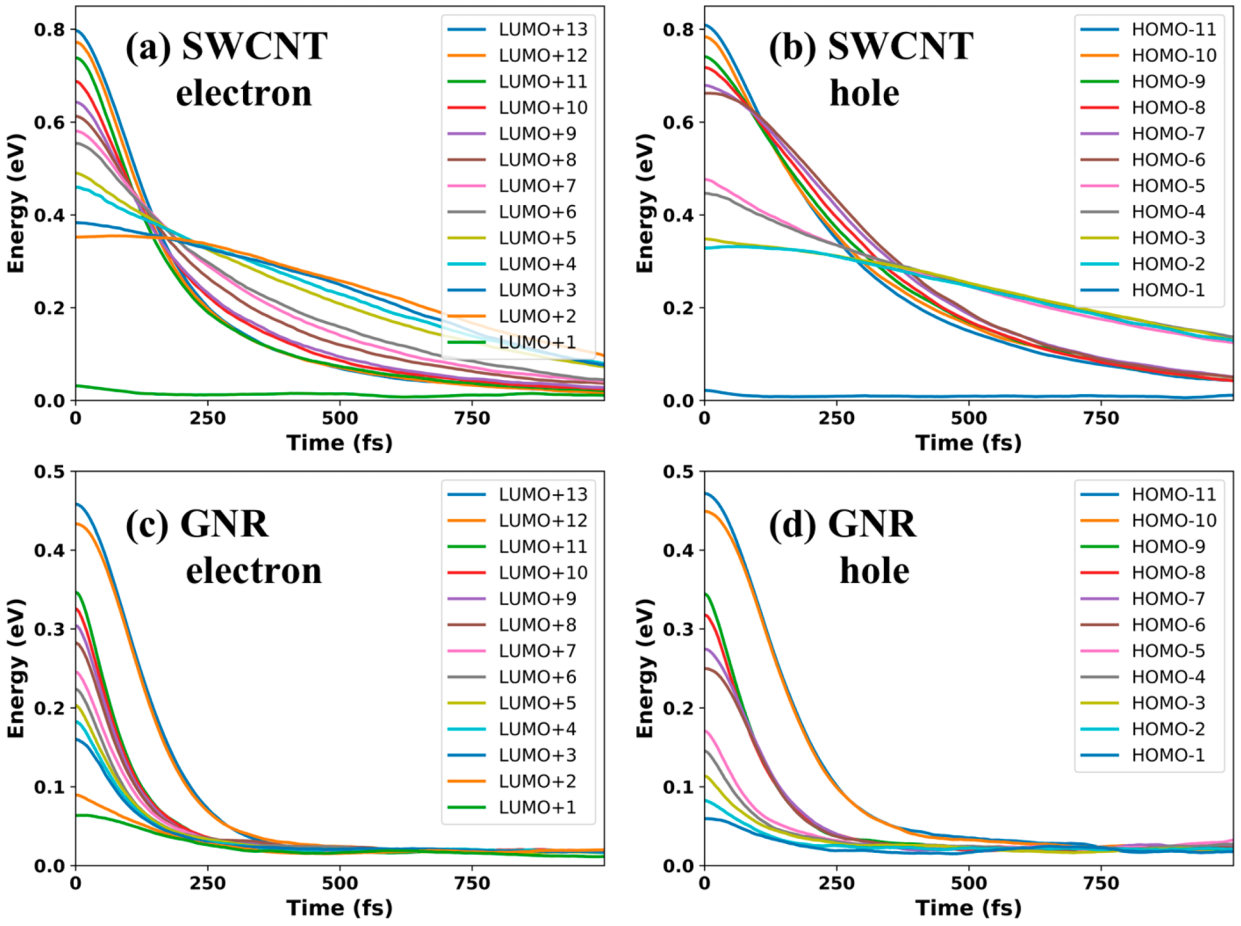

Figure 3. Intraband relaxation of hot electrons and holes to the band edges in the (6,5) SWCNT and GNR with different initial excitations. The zero of energy is set to the corresponding band edge. The relaxation is significantly faster in the GNR than in the SWCNT.

are larger than geometry changes due to photoexcitation. The CPA is essential for modeling systems involving hundreds of atoms over picosecond time scales.

A detailed description of the simulation methodology can be found in ref 55 and 56, which are based on earlier work.[54,61] The approach has been used successfully over a broad range of systems,[61−73] showing good agreement with corresponding experiments and providing a detailed atomistic description of complex quantum dynamics in nanoscale materials.

The geometric and electronic structure of the optimized SWCNT and GNR exhibit many similarities (Figure 1). Both systems are periodic in one dimension. Their bandgaps are on the order of 1 eV and are larger for the GNR. The valence and conduction band DOS show analogous structure in the two systems, increasing away from the bandgap and showing peaks, known as van Hove singularities in SWCNTs. The main qualitative difference between the electronic states of the SWCNT and the GNR resides in the presence of light H atoms in the GNR. However, these atoms do not contribute to the electronic states within the relevant energy range, because both SWCNT and GNR are π-conjugated systems. The properties obtained for the optimized geometries suggest that the SWCNT and the GNR should behave very similarly and that the charge carrier lifetime should, perhaps, be longer in the GNR, because it has a larger bandgap.

Consideration of the SWCNT and GNR properties at ambient temperature already demonstrates significant qualitative differences (Figure 2). Both systems experience geometric distortions due to thermal fluctuations; however, the GNR distorts much more than the SWCNT. The GNR planarity is perturbed significantly. The SWCNT is no longer a perfect cylinder either. However, it maintains its shape. Most important for electron−phonon scattering and electrical conductivity, the GNR wave functions become localized, while the SWCNT wave functions are delocalized over the simulation cell even at room temperature. In this regard, the GNR behavior is similar to that of conjugated polymers,[74,75] which exhibit finite effective conjugation lengths at realistic conditions, while the SWCNT is more similar to traditional bulk semiconductors, which maintain periodicity and delocalized wave function over long distances. It is important to note that on length scales longer than the simulation cell, SWCNTs will also experience distortions and bending; however, the curvature of such distortions and the extent of the resulting wave function localization[74] are much larger than for the GNR. The wave function localization in the GNR at 300 K on the length scale shorter than the simulation cell provides an indication of significant electron−vibrational interactions and has a strong effect on charge transport.

The results of Figure 2 demonstrate the importance of finite temperature studies, because the observed effects are absent at 0 K, while they have a strong influence on the properties under investigation. The harmonic approximation near the equilibrium geometry, often used to model electron−phonon interactions, is also expected to fail for the GNR, because

DOI: 10.1021/acs.jpclett.9b02874
J. Phys. Chem. Lett. 2019, 10, 7179−7187

Table 1. Intraband Relaxation Times (fs) for Hot Electrons and Holes in the SWCNT and GNR, Corresponding to the Plots Shown in Figure 3

electron	LUMO+1	+2	+3	+4	+5	+6	+7	+8	+9	+10	+11	+12	+13
SWCNT	193	866	752	627	557	406	367	317	265	242	207	205	206
GNR	310	227	149	135	131	125	124	121	116	114	111	170	166
hole	HOMO−1	−2	−3	−4	−5	−6	−7	−8	−9	−10	−11		
SWCNT	116	1051	1023	824	727	437	420	377	355	328	309		
GNR	232	180	171	144	135	156	148	128	121	199	194		

the harmonic approximation cannot capture the large-scale anharmonic motions illustrated in Figure 2.

Next, we consider intraband charge relaxation, representing experimental photoexcitations at energies larger than the bandgap.[25] We consider 13 initial states for the electron and 11 initial states for the hole (Figure 3). These initial conditions represent photoexcitations up to 0.8 eV away from the band edges of the SWCNT and 0.5 eV for the GNR. The decay curves shown in Figure 3 are fitted with exponents, $A\exp(-t/\tau)$ to obtain the energy decay times reported in Table 1. Note that the fitting function contains a constant in front of the exponent. The constant accounts for the fact that early time dynamics is always Gaussian, or cosine as in the Rabi oscillation, giving rise to the quantum Zeno effect.[76,77] The evolution becomes exponential only when the wave function spreads over many quantum states, for instance as required during derivation of Fermi's golden rule. The simulation results show that the electron−phonon scattering is significantly slower in the SWCNT than the GNR. Generally, the intraband relaxation is faster for higher initial energies, because the DOS of both SWCNT and GNR increases away from the bandgap. The femtosecond intraband relaxation times obtained in the simulations agree with the carrier scattering times reported in ref 25. Note that there is no direct correspondence between the two sets of data, because the experiments report carrier momentum scattering time obtained from photoconductivity measurements, while calculations obtain energy relaxation times and do not study conductivity, which requires a different type of simulation, e.g., NAMD coupled with the Landauer formalism or with nonequilibrium Green's function theory.[78] The calculations show that charge carriers decay quickly to the band edges in both systems, indicating that after the initial subpicosecond relaxation process, charges are conducted by states near the band edges.

In addition to the intraband charge relaxation, we study the nonradiative electron−hole recombination across the bandgap. The recombination processes eliminate the charges and make electrical conductivity decay to zero. The recombination time scales reported in Table 2 are obtained by fitting the decay of the excited-state population to the exponent. Table 2 also reports the average absolute NA coupling and the pure-dephasing times. Note that the uncertainty in the NA coupling characterizes its fluctuation along the MD trajectories, rather than an error. The uncertainty is on the order of the NA coupling value itself, because the NA couplings fluctuate significantly. The pure-dephasing times characterize elastic charge−phonon scattering taking place during the nonradiative charge recombination. The pure-dephasing times may be loosely compared with the charge momentum scattering times reported in ref 25, because both time scales represent changes in wave function phase. Both pure-dephasing and momentum scattering are faster in the GNR.

Table 2. Electron−Hole Recombination Times, Pure-Dephasing Times, and Average Absolute NA Coupling in the SWCNT and GNR

SWCNT	recombination (ps)	54.0
	dephasing (fs)	76.9
	NA coupling (meV)	3.7 ± 2.4
GNR	recombination (ps)	1.02
	dephasing (fs)	54.8
	NA coupling (meV)	122 ± 105

The nonradiative electron−hole recombination is significantly slower in the SWCNT compared to the GNR, in agreement with the photoconductivity decay measurements.[25] The decay is faster in the GNR because of the much larger NA electron−phonon coupling. The 1 ps electron−hole recombination time computed for the GNR matches well the 0.6 ps experimental photoconductivity lifetime obtained using optical-pump THz-probe spectroscopy.[25] The 54 ps recombination time computed for the SWCNT is notably slower than the measured 1.7 ps photoconductivity lifetime. However, as pointed out by Jensen et al.,[25] their conductivity decay time is considerably lower than the photoluminescence lifetimes.[27] Our result is in good agreement with the latter data. It is important to note that the current simulation considers a perfect SWCNT. The excited-state lifetime can decrease significantly in the presense of defects,[2833] such as point defects, kinks, and CNT ends, even when defect concentration is low, because charges can travel over long distances in CNTs, rapidly finding defect sites.

Further insights into the mechanism of charge−phonon relaxation in the (6,5) SWCNT and GNR are provided by Figures 4 and 5, reporting NA couplings and phonon influence spectra, respectively. Comparing the NA couplings, we observe that they are significantly larger for the GNR than the SWCNT, rationalizing the faster dynamics for both intraband and interband processes. Notably, with some exceptions, the NA couplings are significantly larger between nearest neighbor states, as indicated by the larger and brighter squares along the diagonals in Figure 4. This observation applies both to the SWCNT and the GNR.

In order to rationalize the differences between the NA coupling values for the two systems, consider the expression used to compute these matrix elements

$$\mathrm{NAC} = -i\hbar\left\langle \phi_i \middle| \frac{d}{dt} \middle| \phi_j \right\rangle = -i\hbar\langle\phi_i|\nabla_{\mathbf{R}}|\phi_j\rangle\cdot\dot{\mathbf{R}} \quad (1)$$

Equation 1 shows that the NA coupling is large when the velocities, $\dot{\mathbf{R}}$, of the atoms supporting the electron and hole wave functions are large and/or when the matrix element, $\langle\phi_i|\nabla_{\mathbf{R}}|\phi_j\rangle$, is also large. The matrix element, $\langle\phi_i|\nabla_{\mathbf{R}}|\phi_j\rangle$, relies on overlap of the two wave functions. Also, it contains the nuclear gradient operator, $\nabla_{\mathbf{R}}$, and therefore, it characterizes

DOI: 10.1021/acs.jpclett.9b02874
J. Phys. Chem. Lett. 2019, 10, 7179−7187

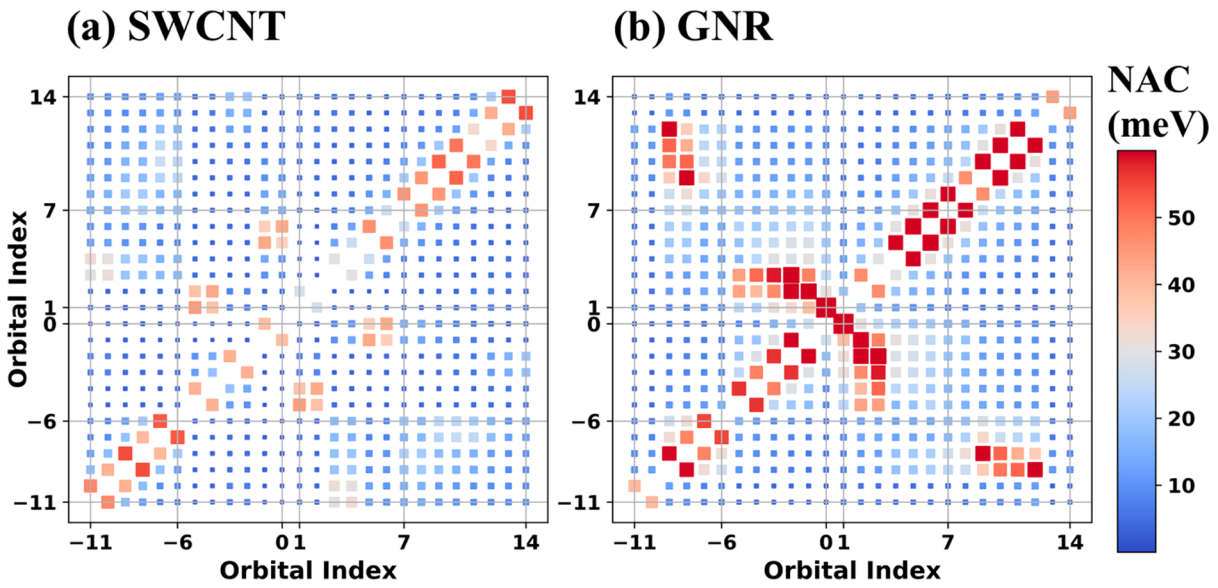

Figure 4. Nonadiabatic coupling (NAC) between Kohn−Sham orbitals in (a) SWCNT and (b) GNR. The orbital indices −11, −6, 0 denote HOMO−11, HOMO−6, and HOMO, respectively, and the indices 1, 7, 14 are for LUMO, LUMO+6, LUMO+13. The size and the color of each square indicate the magnitude of the NAC for the corresponding orbital pair.

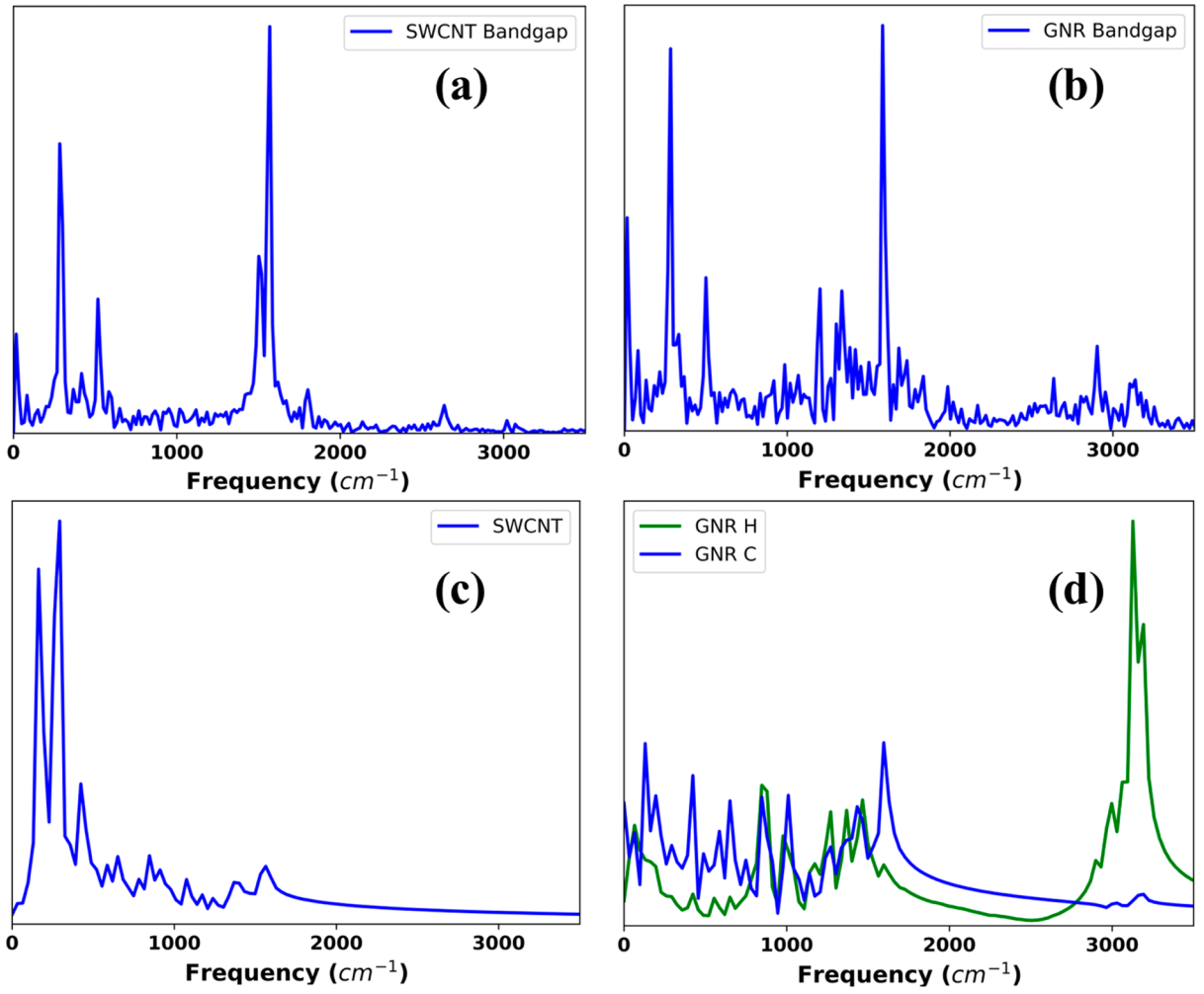

Figure 5. Electron−phonon influence spectra for electron−hole recombination obtained as Fourier transforms (FTs) of the bandgaps for (a) SWCNT and (b) GNR. Charges couple to more phonons in the GNR compared to the SWCNT, including higher-frequency motions, because GNR is more anharmonic and contains light H atoms. Phonon densities of states for (c) SWCNT and (d) GNR computed as FTs of velocity autocorrelation functions. The GNR exhibits higher frequencies than the SWCNT because of the presence of H atoms.

DOI: 10.1021/acs.jpclett.9b02874
J. Phys. Chem. Lett. 2019, 10, 7179−7187

how much electronic wave functions change because of atomic motions.

The GNR is more floppy than the SWCNT, undergoing large-scale fluctuations (Figure 2). In addition, the GNR contains light H atoms. Therefore, the atomic velocities can be higher in the GNR. Even though the charges are supported by the π-electron system of the C atoms, H atoms introduce high-frequency vibrations and high velocities, which may contribute to the electron−phonon couping in the GNR (Figure 5). Considering the nuclear gradient matrix element, $\langle\phi_i|\nabla_{\mathbf{R}}|\phi_j\rangle$, note that GNR motions localize the electron and hole wave functions in the same place (Figure 2). The place where the wave functions are localized changes along the MD trajectory, indicating that the wave functions are quite sensitive to atomic motions, especially compared to the SWCNT. Therefore, the matrix elements, $\langle\phi_i|\nabla_{\mathbf{R}}|\phi_j\rangle$, are much larger in the GNR than the SWCNT. Thus, contributions of both the nuclear gradient matrix element and the atomic velocity to the NA coupling, eq 1, are larger for the GNR, rationalizing the faster charge relaxation and recombination.

Figure 5a,b reports the electron−phonon influence spectra, also known as spectral densities, for the electron−hole recombination in the SWCNT and GNR. The spectra are computed as Fourier transforms (FTs) of the bandgap fluctuations along the MD trajectories. These spectral densities characterize the phonon modes that promote the nonradiative charge recombination. For reference, Figure 5c,d presents FTs of velocity autocorrelation functions averaged over all atoms of the same type in the two systems. The velocity FTs show all phonon modes available in the systems, including those that are not coupled to the charge dynamics.

The nonradiative electron−hole recombination in the SWCNT is promoted most strongly by the G-mode around 1600 cm^{-1} arising from C−C stretching, as well as by the RBMs in the 300−600 cm^{-1} frequency range (Figure 5a). Similar frequencies appear in the GNR influence spectrum (Figure 5b). Note that GNRs do not contain RBMs. An equivalent motion corresponds to GNR distortions (see Figure 2). Comparison of panels a and b of Figure 5 shows that the nonradiative charge recombination in the GNR is facilitated by a broader range of vibrational motions, including significant signals near 3000 cm^{-1}, corresponding to motions of the light H atoms. Interestingly, SWCNT RBMs contribute much more strongly to the velocity FT (Figure 5c) than the influence spectrum (Figure 5a). Even though the number of available higher-frequency modes is smaller than the number of RBMs, the higher-frequency modes correspond to lighter effective masses, have larger velocities ($\dot{\mathbf{R}}$), and create stronger electron−phonon coupling (eq 1). The velocity FT for the C atoms in the GNR is much more even across the 0−1600 cm^{-1} frequency range (Figure 5d) compared to the SWCNT (Figure 5c). All these modes contribute to the nonradiative charge recombination in the GNR (Figure 5)b.

In summary, we have used the state-of-the-art time-domain simulation methodology developed in our group, combining NAMD with real-time TDDFT, to study charge−phonon scattering in SWCNT and GNR of similar size. We have considered both intraband relaxation of hot electrons and holes, and interband electron−hole recombination, and have shown that these processes are significantly faster in the GNR than in SWCNT. The NA electron−phonon coupling is stronger in the GNR by an order of magnitude because of the different rigidities of these, seemingly nearly identical, systems. The electronic properties of the GNR and SWCNT are indeed very similar at 0 K, as suggested by the quantum confinement arguments. However, the GNR undergoes much more significant geometry distortions at room temperature than the SWCNT. As a result, the electron and hole wave functions become localized, symmetry selection rules for the electron−phonon interactions are relaxed, and the electron−phonon coupling becomes much stronger. The presence of light H atoms at GNR edges enhances electron−phonon interactions further. Even though electrons and holes are supported by the π-electron system of C atoms, H atoms couple to carbons and contribute high-frequency modes. Showing good agreement with the time-resolved photoluminescence and photoconductivity measurements, the reported results demonstrate that medium size GNRs with relevant bandgaps behave more as molecules than graphene, while SWCNTs do exhibit extended bulk-like features. The unique time-domain atomistic insights into the complex, nonequilibrium charge−phonon dynamics generated by the simulations modify the traditional view of these graphene nanostructures and suggest that their performance can be tuned by controlling not only size and chemical composition but also structure and rigidity.

AUTHOR INFORMATION

Corresponding Authors

*E-mail: deng@gznc.edu.cn (M.D.).
*E-mail: prezhdo@usc.edu (O.V.P.).

ORCID

Guoqing Zhou: 0000-0002-4000-8467
Mingsen Deng: 0000-0002-3331-3850
Oleg V. Prezhdo: 0000-0002-5140-7500

Notes

The authors declare no competing financial interest.

ACKNOWLEDGMENTS

G.Z. and O.V.P. acknowledge support of the US National Science Foundation (Grant # CHE-1900510). C.C., S.W., and M.D. acknowledge support of the National Natural Science Foundation of China (No. 21763007) and the Hundred Talents Program of Guizhou Province (No. QKH-PTRC[2016]5675).

REFERENCES

(1) Novoselov, K. S.; Geim, A. K.; Morozov, S. V.; Jiang, D.; Zhang, Y.; Dubonos, S. V.; Grigorieva, I. V.; Firsov, A. A. Electric Field Effect in Atomically Thin Carbon Films. *Science* **2004**, *306*, 666−669.

(2) Yu, D. S.; Dai, L. M. Self-Assembled Graphene/Carbon Nanotube Hybrid Films for Supercapacitors. *J. Phys. Chem. Lett.* **2010**, *1*, 467−470.

(3) Castro Neto, A. H.; Guinea, F.; Peres, N. M. R.; Novoselov, K. S.; Geim, A. K. The Electronic Properties of Graphene. *Rev. Mod. Phys.* **2009**, *81*, 109−162.

(4) Xiang, Q. J.; Yu, J. G. Graphene-Based Photocatalysts for Hydrogen Generation. *J. Phys. Chem. Lett.* **2013**, *4*, 753−759.

(5) Iijima, S.; Ichihashi, T. Single-Shell Carbon Nanotubes of 1-Nm Diameter. *Nature* **1993**, *363*, 603−605.

(6) Bolotin, K. I.; Sikes, K. J.; Jiang, Z.; Klima, M.; Fudenberg, G.; Hone, J.; Kim, P.; Stormer, H. Ultrahigh Electron Mobility in Suspended Graphene. *Solid State Commun.* **2008**, *146*, 351−355.

(7) Bachilo, S. M.; Strano, M. S.; Kittrell, C.; Hauge, R. H.; Smalley, R. E.; Weisman, R. B. Structure-Assigned Optical Spectra of Single-Walled Carbon Nanotubes. *Science* **2002**, *298*, 2361−2366.

(8) Novoselov, K. S.; Geim, A. K.; Morozov, S.; Jiang, D.; Katsnelson, M. I.; Grigorieva, I.; Dubonos, S.; Firsov, A. A. Two-

DOI: 10.1021/acs.jpclett.9b02874
J. Phys. Chem. Lett. 2019, 10, 7179−7187

Dimensional Gas of Massless Dirac Fermions in Graphene. *Nature* **2005**, *438*, 197.
(9) Kane, C. L.; Mele, E. J. Quantum Spin Hall Effect in Graphene. *Phys. Rev. Lett.* **2005**, *95*, 226801.
(10) Dai, H. J. Carbon Nanotubes: Synthesis, Integration, and Properties. *Acc. Chem. Res.* **2002**, *35*, 1035−1044.
(11) Zhang, Y.; Tan, Y.-W.; Stormer, H. L.; Kim, P. Experimental Observation of the Quantum Hall Effect and Berry's Phase in Graphene. *Nature* **2005**, *438*, 201.
(12) McEuen, P. L.; Fuhrer, M. S.; Park, H. Single-Walled Carbon Nanotube Electronics. *IEEE Trans. Nanotechnol.* **2002**, *1*, 78−85.
(13) Park, S.; Vosguerichian, M.; Bao, Z. A Review of Fabrication and Applications of Carbon Nanotube Film-Based Flexible Electronics. *Nanoscale* **2013**, *5*, 1727−1752.
(14) Rakhi, R. Preparation and Properties of Manipulated Carbon Nanotube Composites and Applications. In *Nanocarbon and Its Composites*; Elsevier, 2019; pp 489−520.
(15) Allen, M. J.; Tung, V. C.; Kaner, R. B. Honeycomb Carbon: A Review of Graphene. *Chem. Rev.* **2010**, *110*, 132−145.
(16) Jia, X.; Campos-Delgado, J.; Terrones, M.; Meunier, V.; Dresselhaus, M. S. Graphene Edges: A Review of Their Fabrication and Characterization. *Nanoscale* **2011**, *3*, 86−95.
(17) Chen, Y.-C.; De Oteyza, D. G.; Pedramrazi, Z.; Chen, C.; Fischer, F. R.; Crommie, M. F. Tuning the Band Gap of Graphene Nanoribbons Synthesized from Molecular Precursors. *ACS Nano* **2013**, *7*, 6123−6128.
(18) Strano, M. S.; Dyke, C. A.; Usrey, M. L.; Barone, P. W.; Allen, M. J.; Shan, H.; Kittrell, C.; Hauge, R. H.; Tour, J. M.; Smalley, R. E. Electronic Structure Control of Single-Walled Carbon Nanotube Functionalization. *Science* **2003**, *301*, 1519−1522.
(19) Sun, D. M.; Liu, C.; Ren, W. C.; Cheng, H. M. A Review of Carbon Nanotube-and Graphene-Based Flexible Thin-Film Transistors. *Small* **2013**, *9*, 1188−1205.
(20) Lee, S.-H.; Sridhar, V.; Jung, J.-H.; Karthikeyan, K.; Lee, Y.-S.; Mukherjee, R.; Koratkar, N.; Oh, I.-K. Graphene−Nanotube−Iron Hierarchical Nanostructure as Lithium Ion Battery Anode. *ACS Nano* **2013**, *7*, 4242−4251.
(21) Zhao, M.-Q.; Liu, X.-F.; Zhang, Q.; Tian, G.-L.; Huang, J.-Q.; Zhu, W.; Wei, F. Graphene/Single-Walled Carbon Nanotube Hybrids: One-Step Catalytic Growth and Applications for High-Rate Li−S Batteries. *ACS Nano* **2012**, *6*, 10759−10769.
(22) Lin, J.; Peng, Z.; Xiang, C.; Ruan, G.; Yan, Z.; Natelson, D.; Tour, J. M. Graphene Nanoribbon and Nanostructured Sno2 Composite Anodes for Lithium Ion Batteries. *ACS Nano* **2013**, *7*, 6001−6006.
(23) Dillon, A. C.; Jones, K.; Bekkedahl, T.; Kiang, C.; Bethune, D.; Heben, M. Storage of Hydrogen in Single-Walled Carbon Nanotubes. *Nature* **1997**, *386*, 377.
(24) Lee, H.; Ihm, J.; Cohen, M. L.; Louie, S. G. Calcium-Decorated Graphene-Based Nanostructures for Hydrogen Storage. *Nano Lett.* **2010**, *10*, 793−798.
(25) Jensen, S. A.; Ulbricht, R.; Narita, A.; Feng, X.; Müllen, K.; Hertel, T.; Turchinovich, D.; Bonn, M. Ultrafast Photoconductivity of Graphene Nanoribbons and Carbon Nanotubes. *Nano Lett.* **2013**, *13*, 5925−5930.
(26) Zhu, Z.; Crochet, J.; Arnold, M. S.; Hersam, M. C.; Ulbricht, H.; Resasco, D.; Hertel, T. Pump-Probe Spectroscopy of Exciton Dynamics in (6,5) Carbon Nanotubes. *J. Phys. Chem. C* **2007**, *111*, 3831−3835.
(27) Hertel, T.; Himmelein, S.; Ackermann, T.; Stich, D.; Crochet, J. Diffusion Limited Photoluminescence Quantum Yields in 1-D Semiconductors: Single-Wall Carbon Nanotubes. *ACS Nano* **2010**, *4*, 7161−7168.
(28) Kim, Y.; Velizhanin, K. A.; He, X. W.; Sarpkaya, I.; Yomogida, Y.; Tanaka, T.; Kataura, H.; Doorn, S. K.; Htoon, H. Photoluminescence Intensity Fluctuations and Temperature-Dependent Decay Dynamics of Individual Carbon Nanotube Sp(3) Defects. *J. Phys. Chem. Lett.* **2019**, *10*, 1423−1430.
(29) Figueroa del Valle, D. G.; Moretti, L.; Maqueira-Albo, I.; Aluicio-Sarduy, E.; Kriegel, I.; Lanzani, G.; Scotognella, F. Ultrafast Hole Transfer from (6,5) Swcnt to P3ht:Pcbm Blend by Resonant Excitation. *J. Phys. Chem. Lett.* **2016**, *7*, 3353−3358.
(30) Mann, C.; Hertel, T. 13 Nm Exciton Size in (6,5) Single-Wall Carbon Nanotubes. *J. Phys. Chem. Lett.* **2016**, *7*, 2276−2280.
(31) Castillo, M.; Pho, C.; Naumov, A. V.; Dzyuba, S. V. Modulating Chirality-Selective Photoluminescence of Single-Walled Carbon Nanotubes by Ionic Liquids. *J. Phys. Chem. Lett.* **2018**, *9*, 6689−6694.
(32) Kryjevski, A.; Mihaylov, D.; Kilin, D. Dynamics of Charge Transfer and Multiple Exciton Generation in the Doped Silicon Quantum Dot-Carbon Nanotube System: Density Functional Theory-Based Computation. *J. Phys. Chem. Lett.* **2018**, *9*, 5759−5764.
(33) Habenicht, B. F.; Prezhdo, O. V. Nonradiative Quenching of Fluorescence in a Semiconducting Carbon Nanotube: A Time-Domain Ab Initio Study. *Phys. Rev. Lett.* **2008**, *100*, 197402.
(34) Chaban, V. V.; Pal, S.; Prezhdo, O. V. Laser-Induced Explosion of Nitrated Carbon Nanotubes: Nonadiabatic and Reactive Molecular Dynamics Simulations. *J. Am. Chem. Soc.* **2016**, *138*, 15927−15934.
(35) Lauret, J. S.; Voisin, C.; Cassabois, G.; Delalande, C.; Roussignol, P.; Jost, O.; Capes, L. Ultrafast Carrier Dynamics in Single-Wall Carbon Nanotubes. *Phys. Rev. Lett.* **2003**, *90*, 057404.
(36) Pal, S.; Casanova, D.; Prezhdo, O. V. Effect of Aspect Ratio on Multiparticle Auger Recombination in Single-Walled Carbon Nanotubes: Time Domain Atomistic Simulation. *Nano Lett.* **2018**, *18*, 58−63.
(37) Ulbricht, R.; Hendry, E.; Shan, J.; Heinz, T. F.; Bonn, M. Carrier Dynamics in Semiconductors Studied with Time-Resolved Terahertz Spectroscopy. *Rev. Mod. Phys.* **2011**, *83*, 543−586.
(38) Pal, S.; Trivedi, D. J.; Akimov, A. V.; Aradi, B.; Frauenheim, T.; Prezhdo, O. V. Nonadiabatic Molecular Dynamics for Thousand Atom Systems: A Tight-Binding Approach toward Pyxaid. *J. Chem. Theory Comput.* **2016**, *12*, 1436−1448.
(39) Sarkar, R.; Habib, M.; Pal, S.; Prezhdo, O. V. Ultrafast, Asymmetric Charge Transfer and Slow Charge Recombination in Porphyrin/Cnt Composites Demonstrated by Time-Domain Atomistic Simulation. *Nanoscale* **2018**, *10*, 12683−12694.
(40) Xiong, W. J.; Du, L. L.; Lo, K. C.; Shi, H. T.; Takaya, T.; Iwata, K.; Chan, W. K.; Phillips, D. L. Control of Electron Flow Direction in Photoexcited Cycloplatinated Complex Containing Conjugated Polymer-Single-Walled Carbon Nanotube Hybrids. *J. Phys. Chem. Lett.* **2018**, *9*, 3819−3824.
(41) Long, R.; Casanova, D.; Fang, W. H.; Prezhdo, O. V. Donor Acceptor Interaction Determines the Mechanism of Photoinduced Electron Injection from Graphene Quantum Dots into Tio2:Pi-Stacking Supersedes Covalent Bonding. *J. Am. Chem. Soc.* **2017**, *139*, 2619−2629.
(42) Habenicht, B. F.; Craig, C. F.; Prezhdo, O. V. Time-Domain Ab Initio Simulation of Electron and Hole Relaxation Dynamics in a Single-Wall Semiconducting Carbon Nanotube. *Phys. Rev. Lett.* **2006**, *96*, 187401.
(43) Hertel, T.; Moos, G. Electron-Phonon Interaction in Single-Wall Carbon Nanotubes: A Time-Domain Study. *Phys. Rev. Lett.* **2000**, *84*, 5002.
(44) Tully, J. C.; Preston, R. K. Trajectory Surface Hopping Approach to Nonadiabatic Molecular Collisions - Reaction of H+ with D2. *J. Chem. Phys.* **1971**, *55*, 562.
(45) Tully, J. C. Molecular-Dynamics with Electronic-Transitions. *J. Chem. Phys.* **1990**, *93*, 1061−1071.
(46) Bittner, E. R.; Rossky, P. J. Quantum Decoherence in Mixed Quantum-Classical Systems - Nonadiabatic Processes. *J. Chem. Phys.* **1995**, *103*, 8130−8143.
(47) Prezhdo, O. V.; Rossky, P. J. Mean-Field Molecular Dynamics with Surface Hopping. *J. Chem. Phys.* **1997**, *107*, 825−834.
(48) Prezhdo, O. V. Mean Field Approximation for the Stochastic Schrodinger Equation. *J. Chem. Phys.* **1999**, *111*, 8366−8377.
(49) Wang, L. J.; Akimov, A.; Prezhdo, O. V. Recent Progress in Surface Hopping: 2011−2015. *J. Phys. Chem. Lett.* **2016**, *7*, 2100−2112.

DOI: 10.1021/acs.jpclett.9b02874
J. Phys. Chem. Lett. 2019, 10, 7179−7187

(50) Jaeger, H. M.; Fischer, S.; Prezhdo, O. V. Decoherence-Induced Surface Hopping. *J. Chem. Phys.* **2012**, *137*, 22A545.
(51) Akimov, A. V.; Long, R.; Prezhdo, O. V. Coherence Penalty Functional: A Simple Method for Adding Decoherence in Ehrenfest Dynamics. *J. Chem. Phys.* **2014**, *140*, 194107.
(52) Brooksby, C.; Prezhdo, O. V. Quantized Mean-Field Approximation. *Chem. Phys. Lett.* **2001**, *346*, 463−469.
(53) Wang, L. J.; Trivedi, D.; Prezhdo, O. V. Global Flux Surface Hopping Approach for Mixed Quantum-Classical Dynamics. *J. Chem. Theory Comput.* **2014**, *10*, 3598−3605.
(54) Craig, C. F.; Duncan, W. R.; Prezhdo, O. V. Trajectory Surface Hopping in the Time-Dependent Kohn-Sham Approach for Electron-Nuclear Dynamics. *Phys. Rev. Lett.* **2005**, *95*, 163001.
(55) Akimov, A. V.; Prezhdo, O. V. The Pyxaid Program for Non-Adiabatic Molecular Dynamics in Condensed Matter Systems. *J. Chem. Theory Comput.* **2013**, *9*, 4959−4972.
(56) Akimov, A. V.; Prezhdo, O. V. Advanced Capabilities of the Pyxaid Program: Integration Schemes, Decoherenc:E Effects, Multi-excitonic States, and Field-Matter Interaction. *J. Chem. Theory Comput.* **2014**, *10*, 789−804.
(57) Kresse, G.; Furthmuller, J. Efficient Iterative Schemes for Ab Initio Total-Energy Calculations Using a Plane-Wave Basis Set. *Phys. Rev. B: Condens. Matter Mater. Phys.* **1996**, *54*, 11169−11186.
(58) Perdew, J. P.; Burke, K.; Ernzerhof, M. Generalized Gradient Approximation Made Simple. *Phys. Rev. Lett.* **1996**, *77*, 3865−3868.
(59) Blochl, P. E. Projector Augmented-Wave Method. *Phys. Rev. B: Condens. Matter Mater. Phys.* **1994**, *50*, 17953−17979.
(60) Akimov, A. V.; Prezhdo, O. V. Persistent Electronic Coherence Despite Rapid Loss of Electron-Nuclear Correlation. *J. Phys. Chem. Lett.* **2013**, *4*, 3857−3864.
(61) Li, L. Q.; Long, R.; Prezhdo, O. V. Why Chemical Vapor Deposition Grown Mos2 Samples Outperform Physical Vapor Deposition Samples: Time-Domain Ab Initio Analysis. *Nano Lett.* **2018**, *18*, 4008−4014.
(62) He, J. L.; Vasenko, A. S.; Long, R.; Prezhdo, O. V. Halide Composition Controls Electron-Hole Recombination in Cesium-Lead Halide Perovskite Quantum Dots: A Time Domain Ab Lnitio Study. *J. Phys. Chem. Lett.* **2018**, *9*, 1872−1879.
(63) Zhang, L. L.; Vasenko, A. S.; Zhao, J.; Prezhdo, O. V. Mono-Elemental Properties of 2d Black Phosphorus Ensure Extended Charge Carrier Lifetimes under Oxidation: Time-Domain Ab Initio Analysis. *J. Phys. Chem. Lett.* **2019**, *10*, 1083−1091.
(64) Jankowska, J.; Prezhdo, O. V. Real-Time Atomistic Dynamics of Energy Flow in an Stm Setup: Revealing the Mechanism of Current-Induced Molecular Emission. *J. Phys. Chem. Lett.* **2018**, *9*, 3591−3597.
(65) Li, W.; Long, R.; Hou, Z. F.; Tang, J. F.; Prezhdo, O. V. Influence of Encapsulated Water on Luminescence Energy, Line Width, and Lifetime of Carbon Nanotubes: Time Domain Ab Initio Analysis. *J. Phys. Chem. Lett.* **2018**, *9*, 4006−4013.
(66) Li, W.; Long, R.; Tang, J. F.; Prezhdo, O. V. Influence of Defects on Excited-State Dynamics in Lead Halide Perovskites: Time-Domain Ab Initio Studies. *J. Phys. Chem. Lett.* **2019**, *10*, 3788−3804.
(67) Wang, Y. T.; Fang, W. H.; Long, R.; Prezhdo, O. V. Symmetry Breaking at Mapbi(3) Perovskite Grain Boundaries Suppresses Charge Recombination: Time-Domain Ab Initio Analysis. *J. Phys. Chem. Lett.* **2019**, *10*, 1617−1623.
(68) Liu, L. H.; Fang, W. H.; Long, R.; Prezhdo, O. V. Lewis Base Passivation of Hybrid Halide Perovskites Slows Electron-Hole Recombination: Time-Domain Ab Lnitio Analysis. *J. Phys. Chem. Lett.* **2018**, *9*, 1164−1171.
(69) Zhang, Z. S.; Liu, L. H.; Fang, W. H.; Long, R.; Tokina, M. V.; Prezhdo, O. V. Plasmon-Mediated Electron Injection from Au Nanorods into Mos2: Traditional Versus Photoexcitation Mechanism. *Chem.* **2018**, *4*, 1112−1127.
(70) Fischer, S. A.; Duncan, W. R.; Prezhdo, O. V. Ab Initio Nonadiabatic Molecular Dynamics of Wet-Electrons on the Tio2 Surface. *J. Am. Chem. Soc.* **2009**, *131*, 15483−15491.
(71) Kilin, D. S.; Tsemekhman, K.; Prezhdo, O. V.; Zenkevich, E. I.; von Borczyskowski, C. Ab Initio Study of Exciton Transfer Dynamics from a Core-Shell Semiconductor Quantum Dot to a Porphyrin-Sensitizer. *J. Photochem. Photobiol., A* **2007**, *190*, 342−351.
(72) Wang, L. J.; Long, R.; Prezhdo, O. V. Time-Domain Ab Initio Modeling of Photoinduced Dynamics at Nanoscale Interfaces. *Annu. Rev. Phys. Chem.* **2015**, *66*, 549.
(73) Akimov, A. V.; Asahi, R.; Jinnouchi, R.; Prezhdo, O. V. What Makes the Photocatalytic Co2 Reduction on N-Doped Ta2o5 Efficient: Insights from Nonadiabatic Molecular Dynamics. *J. Am. Chem. Soc.* **2015**, *137*, 11517−11525.
(74) Kilina, S.; Kilin, D.; Tretiak, S. Light-Driven and Phonon-Assisted Dynamics in Organic and Semiconductor Nanostructures. *Chem. Rev.* **2015**, *115*, 5929−5978.
(75) Nayyar, I. H.; Batista, E. R.; Tretiak, S.; Saxena, A.; Smith, D. L.; Martin, R. L. Localization of Electronic Excitations in Conjugated Polymers Studied by Dft. *J. Phys. Chem. Lett.* **2011**, *2*, 566−571.
(76) Kilina, S. V.; Neukirch, A. J.; Habenicht, B. F.; Kilin, D. S.; Prezhdo, O. V. Quantum Zeno Effect Rationalizes the Phonon Bottleneck in Semiconductor Quantum Dots. *Phys. Rev. Lett.* **2013**, *110*, 180404.
(77) Prezhdo, O. V. Quantum Anti-Zeno Acceleration of a Chemical Reaction. *Phys. Rev. Lett.* **2000**, *85*, 4413−4417.
(78) Xue, Y. Q.; Datta, S.; Ratner, M. A. First-Principles Based Matrix Green's Function Approach to Molecular Electronic Devices: General Formalism. *Chem. Phys.* **2002**, *281*, 151−170.

DOI: 10.1021/acs.jpclett.9b02874
J. Phys. Chem. Lett. 2019, 10, 7179−7187